Materials Science and Engineering A 499 (2009) 387–395

Contents lists available at ScienceDirect

Materials Science and Engineering A

journal homepage: www.elsevier.com/locate/msea

Aging-dependent coupling effect of multiple precipitates on the ductile fracture of heat-treatable aluminum alloys

S.P. Yuan [a], G. Liu [a], R.H. Wang [a], G.-J. Zhang [a], X. Pu [a], J. Sun [a,*], K.-H. Chen [b]

[a] State Key Laboratory for Mechanical Behavior of Materials, School of Material Science & Engineering, Xi'an Jiaotong University, Xi'an 710049, China
[b] State Key Laboratory for Powder Metallurgy, The University of Southern Central China, Changsha 410083, China

ARTICLE INFO

Article history:
Received 24 April 2008
Received in revised form 17 August 2008
Accepted 2 September 2008

Keywords:
Aluminum alloys
Fracture
Multiple precipitates

ABSTRACT

Heat-treatable aluminum alloys usually contain two or more kinds of precipitates but how the macro-properties depend on the multiple precipitates, especially in a quantitative manner, has not been well known. In this paper, systematic experiments and modeling are performed to study the coupling effect of multiple precipitates on the strength and ductility of aged Al–Mg–Si alloys that contain three kinds of precipitates. A density-dependent superposition effect of the multiple precipitates on the ductility, essentially similar to that on the yield strength, is clearly revealed and quantitatively modeled. It is surprisingly found that an appropriate combination of the multiple precipitates could increase the ductility significantly with sacrificing strength less. Calculations are in good agreement with experiments.

1. Introduction

The mechanical properties of heat-treatable aluminum alloys are closely dependent on the aging treatment because the strengthening precipitates are especially sensitive to both the aging temperature (T) and the aging time (t). In order to achieve the artificial controlling of the mechanical properties in aged aluminum alloys to meet the industrial need, there has been increasing interest in establishing quantitative relationships between the mechanical properties and the processing parameters (T and t) of aging treatment directly [1–4]. Many efforts have been made in modeling the aging-dependent yield strength in the heat-treatable aluminum alloys [5–14], where the precipitation kinetics was first quantitatively presented and the strengthening effect was subsequently calculated to understand the dynamic dependence of yield strength on the aging temperature as a function of aging time. The aging-dependent yield strength has been well modeled on different series of aluminum alloys (e.g., 2xxx series or Al–Cu–Mg-based alloys [5,6], 6xxx series or Al–Mg–Si-based alloys [7–10], and 7xxx series or Al–Zn–Mg-based alloys [11]), on different types of strengthening precipitates (shearable type [3] or unshearable type [12,13]), and on different morphologies of strengthening precipitates (sphere [11], rod/needle, or disc/plate [15]). In comparison, there have been much fewer reports on the modeling of aging-dependent ductility and fracture toughness in heat-treatable aluminum alloys, mainly due to the much difficulty in establishing suitable fracture model for the industrial aluminum alloys where multiscale second phase particles are usually coexisted [16–18], i.e., micrometer-sized constituents, submicrometer-sized dispersoids, and nanometer-sized precipitates. Recently, some of the present authors [19–22] have developed a multiscale fracture model to describe the combined effects of multiscale second phase particles on the ductility and fracture toughness in heat-treatable aluminum alloys successfully. Using the multiscale fracture model with our previous aging strengthening model [15], it is possible to provide a comprehensive predictive tool on optimizing combination of yield strength, ductility, and fracture toughness by artificial controlling aging treatment.

Unfortunately, almost all the aforementioned process modeling works were based on a single type of strengthening precipitate for simplification reason. This simple assumption, although providing a relative easy way to understand the aging-dependent mechanical properties quantitatively, usually failed in describing the true case in industrial aluminum alloys. In practice, because of the complex composition and complicated thermal–mechanical treatment, multiple precipitates with different chemical composition, different particle size, and/or different morphology can be commonly observed in aged aluminum alloys [23–29]. For example, multiple precipitates of δ′ phase, θ′ phase, and T_1 phase are coexisted in Al–Cu–Li alloys [23,24], and of β″ phase and Q′ phase in 6xxx series alloys [25–29]. The influence of multiple precipitates on the mechanical properties should be much more complicated than that of a single type of precipitates. Computer simulations

* Corresponding author.
E-mail address: junsun@mail.xjtu.edu.cn (J. Sun).

0921-5093/$ – see front matter © 2008 Elsevier B.V. All rights reserved.
doi:10.1016/j.msea.2008.09.012

and experiments have shown that the combined strengthening effect of multiple second phase particles, especially of multiple precipitates, follows a superposition law, either density-dependent $\tau_t^\alpha = \sum_{i=1}^{N} n_i^{\alpha/2} \tau_i^\alpha$ [30,31] or independent of density $\tau_t^\alpha = \sum_{i=1}^{N} \tau_i^\alpha$ [32–36], where τ_t is the total strengthening shear stress, τ_i is the contribution to the strengthening effect due to the i particles and n_i is the relative density function of i particles ($\sum_{i=1}^{N} n_i = 1$), and the exponent α has the value between 1 (linear addition law) and 2 (Pythagorean addition law). These *ad hoc* superposition expressions have been found to fit favorably with the experimental results on the strengthening effect of multiple precipitates in heat-treatable aluminum alloys (e.g., in Zhu et al.'s work [30]). As to the influence of multiple precipitates on the ductility or ductile fracture, however, few reports have been presented despite of its importance.

Most recently, the present authors [37] have made an attempt to study the influence of multiple precipitates on the ductility of aged aluminum alloys in a quantitative manner. An Al–Mg–Si alloys were quickly pre-aged at somewhat low temperature for a short time, then stored at room temperature for a long time and subsequently secondly aged at 473 K, resulting in the coexistence of three kinds of precipitates different in both composition and morphology. The size and volume fraction of the three kinds of precipitates evolved with aging time, which was believed to be responsible for the remarkable change in ductility (the strain to fracture, ε_f) with aging time. The influence of multiple precipitates on ε_f was crudely revealed to be a density-dependent superposition of the contribution due to the individual type of precipitates, somewhat similar to that on yield strength. This result seems to enhance the deep understanding on the ductile fracture of metal materials containing multiple second phase particles. This preliminary conclusion, however, was drawn only under a specific aging treatment of $T = 473$ K. More experimental and modeling investigations should be needed to make it clear that whether the conclusion of density-dependent superposition effect of multiple precipitates on ductility is universal and operative under other aging temperatures and other combinations of multiple precipitates.

In this paper, systematic experiments and modeling were performed to study the coupling influence of multiple precipitates on the yield strength and ductility in an Al–Mg–Si alloy aged at different temperatures. Especial attention was paid on the establishment of quantitative relationship between the mechanical properties and the aging-dependent evolution of the multiple precipitates. The density-dependent superposition effect of multiple precipitates on both the yield strength and the strain to fracture ε_f was further verified experimentally and theoretically.

2. Experimental procedures

As an important material used in the automobile industry, Al–Mg–Si alloys are usually applied by a two-step aging treatment, where a pre-aging treatment is firstly employed to form "seeds", whereas the effective hardening precipitates will be formed rapidly upon a short time during the subsequent secondary aging treatment in the car manufacturing plants [38,39]. The purpose of the pre-aging treatment is to make the alloys not only be sufficiently soft for good formability but also form certain particles for the quick hardening response upon the second heating. However, due to the reasons such as transportation and storage (up to months), the pre-aged Al–Mg–Si alloys will stay at room temperature for a long time before the second heating, resulting in the complicated precipitation of second phase particles. Here, a similar aging treatment will be employed to follow the industrial process.

The Al–Mg–Si alloys used in present investigation are extruded rods of 18 mm in diameter. The composition in weight percentage is 1.12% Mg, 0.57% Si, 0.25% Cu, and balance Al. The alloys had been solution-treated at 783 K for half-hour followed by water quench and then been pre-aged at 373 K for 20 min. After stored at room temperature for months, the alloys were secondly aged for a series of time from 2 to 40 h at 473 and 523 K, respectively.

The yield strength and strain to fracture of the differently aged alloys were measured by using a smooth dog bone-shaped tensile specimen that had a gauge size of 6 mm in diameter and 40 mm in length. All of the specimens had an axis along the longitudinal direction. The tensile test was performed at a constant strain rate of $5 \times 10^{-4}\ s^{-1}$ with the load direction parallel to the specimen axis. The yield stress was determined as the 0.2% offset and the strain to fracture was determined as $\varepsilon_f = \ln(A_0/A_f)$, where A_0 is the initial area and A_f is the area at fracture of the specimens.

Based on quantitative microscopy, the size and volume fraction of the three kinds of precipitates were quantitatively measured by using transmission electron microscopy (TEM). Thin foil specimens for TEM observation were thinned by electro-polishing with an applied potential of 15 V in a nitric acid–methanol solution with the ratio of 1:3 at 253 K, and subsequently cleaned by Ar^+ ions to remove oxide layers. The composition and structural analysis were conducted on field emission TEM (JEOL JEM-2100F) operated at 200 kV. The volume fraction of precipitates in a thin foil project (corrected for truncation and overlap) was determined by [23]:

$$f = \left(\frac{-2\pi r}{\pi r + 4\varsigma}\right) \ln(1 - S_A) \quad (1)$$

where r is the radius of the spherical precipitates (replaced by l for the rod-shaped or needle-shaped precipitates), ς is the foil thickness and S_A is the projected area fraction of the precipitates, as determined by the point count method. The foil thickness was easily obtained by utilizing a grain boundary fringes technique [40].

3. Experimental results

3.1. Multiple precipitates

Fig. 1(a) typically shows a microstructure of the specimen before secondary artificial aging treatment, where only a kind of spherical precipitates are observed. These spherical precipitates were nucleated during the pre-aging stage and subsequently grew during the following storage period at room temperature. The mean radius of these precipitates is about 15 nm. While after secondary aging treatment, another two types of precipitates can be also observed in the sample, as indicated by arrows in Fig. 1(b). One has a somewhat large size and is in rod shape, while the other is slim and in needle shape. Of special interest to note is that the rod-shaped precipitates were found to nucleate *in situ* on the original spherical precipitates and grow by consuming the latter ones.

The crystal structure of the three kinds of precipitates was examined by using the HRTEM (high resolution transmission electron microscopy) and corresponding FT (Fourier transform) analyses and HRTEM image simulations analyses, respectively. For example, after analyzing several tens of the spherical precipitates by using the HRTEM and corresponding FT analyses, it can be determined that these particles have the same structure of $AlMg_4Si_6$ or pre-β″ phase with lattice constants being $a = 16.53$ Å, $b = 6.63$ Å, $c = 6.72$ Å, and $\beta = 102^\circ$, and space group being $C2/m$ [29]. A HRTEM and corresponding FT image of spherical precipitates are shown in Fig. 2(a). The reflections marked by the green circle in the FT image are originating from the Al matrix, which are coincided with some pre-β″

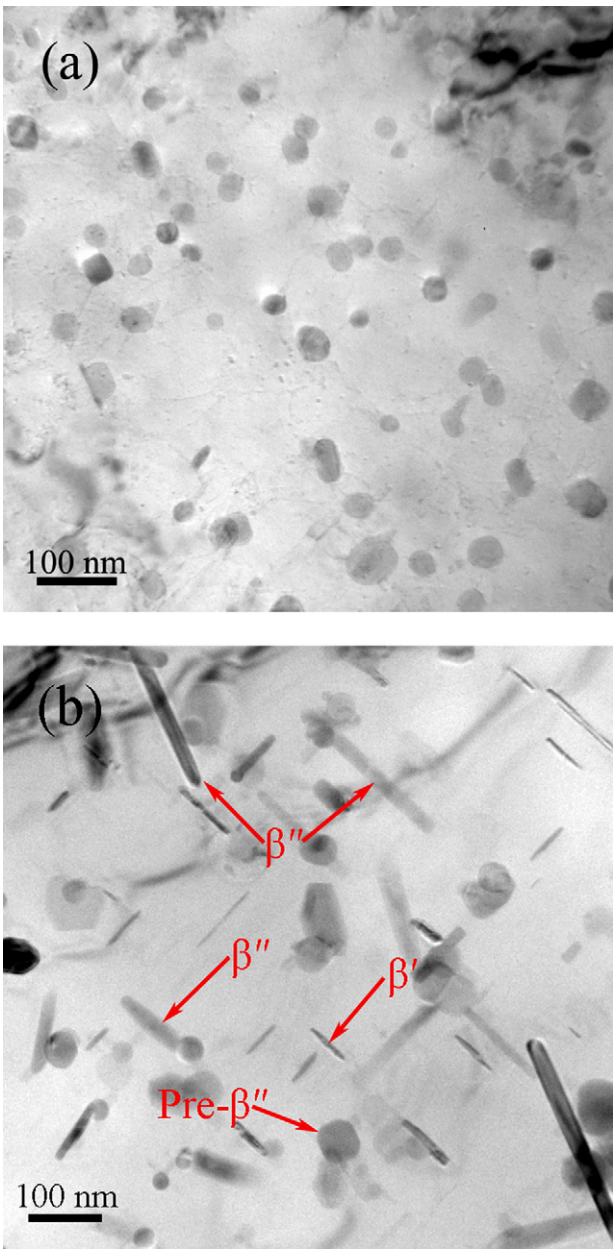

Fig. 1. Typical TEM images showing the morphology and size of pre-β″ precipitates of $AlMg_4Si_6$ before secondary aging treatment (a) and of multiple precipitates, i.e., spherical pre-β″ particles of $AlMg_4Si_6$, rod-shaped β″ precipitates of Mg_5Si_6, and needle-shaped β′ precipitates of Mg_2Si, after secondary aging treatment (b).

reflections. The left image in Fig. 2(b) is a magnified HRTEM image corresponding to the area marked with green rectangle in left of Fig. 2(a). The experimental HRTEM image is recorded along the ⟨0 1 0⟩ direction, consistent with the $AlMg_4Si_6$ atomic model in the right of Fig. 2(b). To verify the structure of the spherical precipitates, HRTEM image simulations [38,41] were carried out for a primary beam energy of 200 kV and a spherical aberration coefficient of Cs = 1.5 mm. The simulated image (inserted in the experimental image and indicated by an arrow in Fig. 2(b)), obtained using a defocus value of $\Delta f = -460$ Å and $AlMg_4Si_6$ atom model, is found in good agreement with the experimental image. Using the same method, the rod-shaped precipitates and the needle-shaped precipitates were determined to be β″ or Mg_5Si_6 phase and β′ or Mg_2Si phase, respectively.

3.2. Growth kinetics of the multiple precipitates

Growth kinetics of the three kinds of precipitates was experimentally examined at T = 473 and 523 K, respectively. Fig. 3 shows the aging time (t)-dependent mean radius (r) and half-length (l) of the rod-shaped β″ precipitates (solid circle dots) and the needle-shaped β′ precipitates (solid diamond dots), respectively, where (a) and (b) correspond to T = 473 K and (c) and (d) to T = 523 K. Fitting lines suggest that all the size variations of the two kinds of precipitates follow a similar expression of $r(l) = At^c$, where aging time t is in h, A is a growth constant, and c is the growth exponent. On the growth of rod-shaped β″ precipitates at T = 473 K, it is determined that A is 4.4 for r and 30 for l, and the growth exponent c is about 0.25. While for the needle-shaped β′ precipitates, somewhat lower constants are found as A = 2.9 for r and 29 for l, and c = 0.1. The lower growth exponent c for the needle-shaped β′ precipitates may be attributed to the reason that most of the excess solute atoms have been precipitated to support the long-time growth of the pre-β″ particles, and the revived excess solute atoms that could be used for the growth of the β′ precipitates were thus much less. On the contrary, the β″ particles grew by directly consuming the pre-β″ particles and so had a faster growth rate.

At higher aging temperature of T = 523 K, both the rod-shaped β″ particles and the needle-shaped β′ precipitates have increased sizes because the atomic diffusion were enhanced at higher temperature. Revealed from Fig. 3(c) and (d), the β″ particles showed the growth constants of A = 6.5 for r and 20 for l, and c = 0.5, and the β′ precipitates had A = 6.5 for r and 36 for l, and c = 0.1.

Because some spherical pre-β″ precipitates were dissolved to provide solute atoms for the growth of rod-shaped β″ precipitates, the volume fraction of spherical pre-β″ precipitates decreased gradually, as typically shown in Fig. 4 where the aging temperature is 523 K. On the contrary, the volume frac-

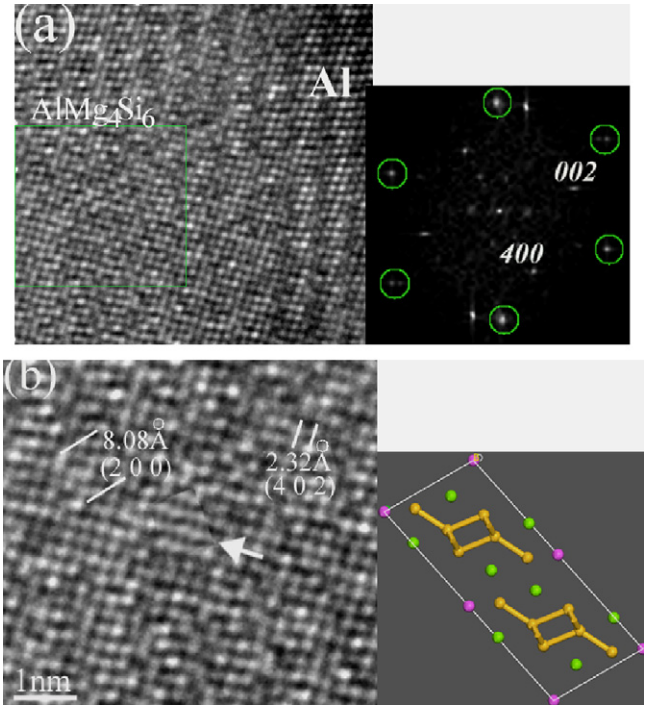

Fig. 2. (a) HRTEM image of the pre-β″ precipitates and corresponding FT image corresponding; (b) magnified image corresponding to the area marked with green rectangle in (a). The simulated image of the $AlMg_4Si_6$ phase is also shown for comparison, as indicated by white arrow. (For interpretation of the references to color in this figure legend, the reader is referred to the web version of the article.)

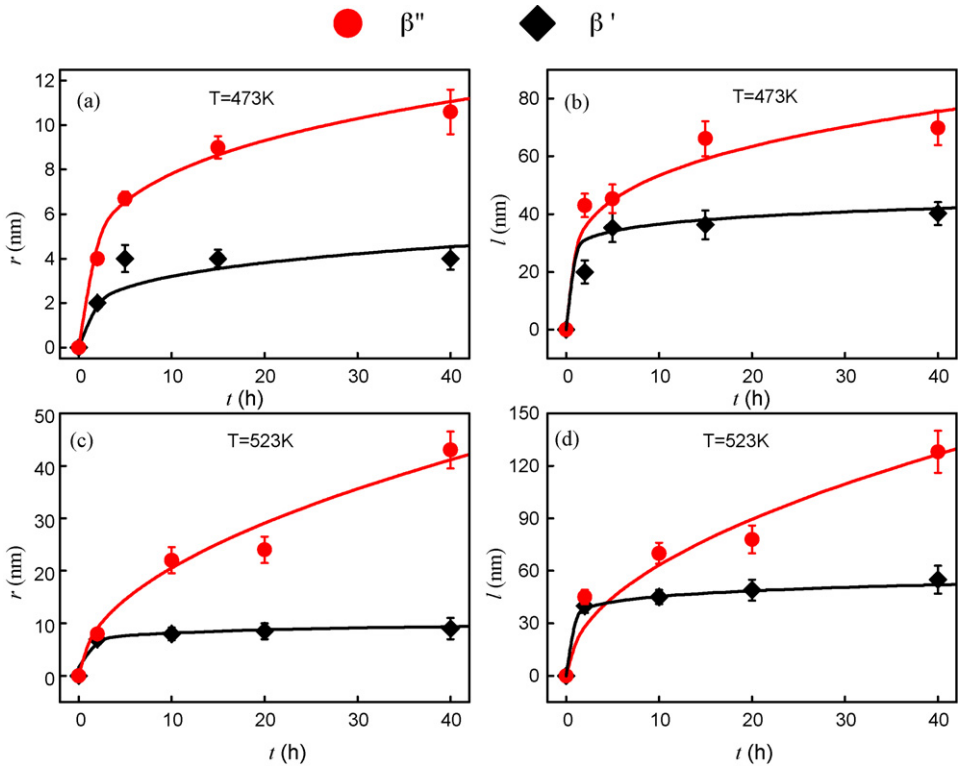

Fig. 3. Variation of the average size (radius r and half-length l) of the β″ precipitates (circle dots) and β′ precipitates (diamond dots) with aging time (t) at T = 473 and 523 K, respectively.

tion of both the β″ precipitates and the β′ precipitates increases sharply at the early aging course and subsequently exhibits somewhat slight change. The saturation in volume fraction of the two precipitates is believed to associate with the entire consumption of the excess solute atoms in matrix as well as the achievement of thermodynamic stability of survived pre-β″ particles. In first approximation, all the volume fraction evolutions of the three kinds of precipitates follow an Avrami type [3,4] or quasi-Avrami type relationship. For example, the spherical pre-β″ precipitates exhibit the time-dependent volume fraction variation as $f_s = 0.89 - 0.37\{1 - \exp[-(t/t_0)^{1.5}]\}$ (t_0 = 16.67 h) at 523 K, while the rod-shaped β″ particles and needle-shaped β′ particles show $f_r = 0.45\{1 - \exp[-(t/t_0)^{1.5}]\}$ (t_0 = 16.67 h) and $f_n = 0.55\{1 - \exp[-(t/t_0)^{1.5}]\}$ (t_0 = 1.67 h), respectively. These isothermal phase transition kinetics curves are closely similar to our previous results on the same Al–Mg–Si alloys [42]. The aging-dependent parameters of the multiple precipitates are summarized in Table 1 and all the fitting lines will be used for subsequent calculations in Section 4.

3.3. Mechanical properties

Corresponding to the variation of multiple precipitates with aging temperature and aging time, the sample exhibited a remarkable change in mechanical properties. Table 2 summarizes the measured yield strength (σ_y) and the strain to fracture (ε_f) of the aged Al–Mg–Si alloys. It is surprisingly found from Table 2 that the yield strength decreases gradually in the secondary aging treatment. This unusual result may be associated with the much long storage at room temperature before the secondary aging treatment. During the storage, the pre-β″ particles that nucleated in the pre-aging treatment grew up to effective strengthening obstacles and had intense strengthening effect. In comparison, the rod-shaped β″ particles and the needle-shaped β′ particles precipitated during

Table 1
Parameter evolution of the three kinds of precipitates.

T (K)/t (h)	Pre-β″	β″				β′			
	f_s (vol%)	r_r (nm)	l_r (nm)	λ_r (nm)	f_r (vol%)	r_n (nm)	l_n (nm)	λ_n (nm)	f_n (vol%)
473									
0	0.89 (±0.05)	0	0	–	0	0	0	–	0
2	0.73 (±0.05)	4 (±0.2)	43 (±4)	106 (±14)	0.37 (±0.05)	2 (±0.2)	20 (±4)	49 (±5)	0.43 (±0.04)
5	0.33 (±0.06)	7 (±0.3)	45 (±5)	158 (±15)	0.33 (±0.04)	4 (±0.6)	35 (±5)	89 (±15)	0.52 (±0.05)
15	0.27 (±0.07)	9 (±0.5)	66 (±6)	209 (±20)	0.38 (±0.07)	4 (±0.4)	36 (±5)	92 (±12)	0.48 (±0.03)
40	0.21 (±0.08)	10.6 (±1)	70 (±6)	242 (±24)	0.36 (±0.06)	4 (±0.5)	40 (±4)	90 (±12)	0.57 (±0.04)
523									
0	0.89 (±0.05)	0	0	–	0	0	0	–	0
2	0.80 (±0.06)	8 (±1)	45 (±4)	237 (±29)	0.14 (±0.03)	7 (±1.5)	40 (±4)	140 (±15)	0.46 (±0.05)
10	0.66 (±0.07)	22 (±2.5)	70 (±6)	394 (±32)	0.36 (±0.04)	8 (±1.2)	45 (±4)	152 (±16)	0.53 (±0.04)
20	0.62 (±0.09)	24 (±2.5)	78 (±8)	422 (±47)	0.39 (±0.05)	8 (±1.5)	49 (±6)	160 (±16)	0.56 (±0.03)
40	0.52 (±0.04)	43 (±3.5)	128 (±12)	706 (±57)	0.44 (±0.04)	9 (±2)	55 (±8)	175 (±22)	0.54 (±0.04)

Table 2
Aging-dependent mechanical properties.

T (K)/t (h)	σ_y (MPa)	ε_f (%)
473		
0	255(±3)	8.5(±0.6)
5	225(±4)	16.9(±1.8)
15	200(±5)	18.8(±1.1)
20	210(±4)	20.0(±1.5)
30	204(±5)	21.4(±2.1)
40	205(±3)	24.8(±2.4)
523		
0	255(±3)	8.5 (±0.6)
2	183(±5)	48.9(±6.2)
5	166(±4)	52.8(±5.2)
10	164(±4)	52.8(±5.6)
20	158(±5)	53.3(±6.2)
30	154(±3)	53.9(±8.4)
40	154(±3)	53.8(±6.5)

the secondary aging treatment have less strengthening effect due to their larger sizes. As a result, the decrease in volume fraction of the pre-β″ particles during the secondary aging treatment caused the reduction in yield strength. On the other hand, ε_f increases with aging time, even up to over six times than the original one at T = 523 K. This indicates that the appropriate combination of the multiple precipitates (from only spherical precipitates to the combination of partial spherical precipitates plus partial rod-shaped and needle-shaped precipitates) could increase the ductility significantly while sacrificing the strength somewhat less, which could be employed to tailor the combination of the multiple precipitates artificially to achieve superior comprehensive mechanical properties.

4. Discussion

The mechanical properties of the present Al–Mg–Si alloys are closely dependent on the evolution of multiple precipitates. In this section, the coupling effect of multiple precipitates on the yield strength and on the ductility or the strain to fracture will be discussed and modeled, respectively. Quantitative analyses reveal that the coupling effect is a density-dependent superposition of the individual kinds of precipitates, which could be used to aid the material design.

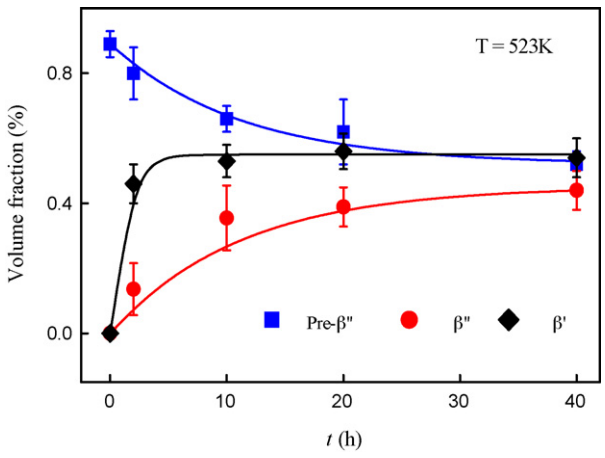

Fig. 4. Variation of the volume fraction (f) of the pre-β″ precipitates (square dots), β″ precipitates (circle dots) and β′ precipitates (diamond dots) with t at T = 523 K. Fitting lines are presented for quantitative description.

4.1. Coupling effect of multiple precipitates on yield strength

Because the constituents and dispersoids contribute much less to the strength, the overall yield strength (σ_y) of the aged aluminum alloys is a sum of the intrinsic strength of pure aluminum (σ_i), the solid solution strengthening (σ_{ss}), and the precipitation hardening (σ_p), i.e.,

$$\sigma_y = \sigma_i + \sigma_{ss} + \sigma_p \tag{2}$$

Because the differently aged-treated alloys in present investigation were found to have the same grain size (about 726 μm in the extrusion direction and 49 μm in radial direction), σ_i can be looked as a constant which has been evaluated in our previous paper [15]. The contribution from the solid solution strengthening, σ_{ss}, is a function of the concentration of the solute atoms in the matrix, C [43]:

$$\sigma_{ss} = \sum_j q_j C_j^{2/3} \tag{3}$$

where j represents specific solute elements Mg, Si and Cu in present Al alloy, C_j is the adding dependent concentration of a specific solute element in solid solution that can be calculated by using the authors' precipitation kinetic model [15], and q_j is the corresponding scaling factor as q_{Mg} = 29.0 MPa/wt%$^{2/3}$, q_{Si} = 66.3 MPa/wt%$^{2/3}$, and q_{Cu} = 46.4 MPa/wt%$^{2/3}$ [7].

The precipitation hardening (σ_p) includes contributions from spherical pre-β″ particles (σ_s), rod-shaped β″ particles (σ_r), and needle-shaped β′ particles (σ_n). Because of the spherical morphology of the pre-β″ particles, σ_s can be given as [7]:

$$\sigma_s = \frac{M}{r_s}(2\psi G b)\left(\frac{3f_s}{2\pi}\right)^{1/2} \tag{4}$$

where M is the Taylor factor (~3.1), G is the shear modulus of the aluminum matrix (28 GPa), b is the magnitude of Burgers vector in Al (0.286 nm), ψ is a constant close to 0.5, and r_s and f_s are mean particle size and volume fraction of the spherical pre-β″ precipitates, respectively. While for the other two non-spherical precipitates, i.e., the rod-shaped β″ precipitates and needle-shaped β′ precipitates, the strengthening contribution could be described by [13,15]:

$$\sigma_{r/n} = 0.065MG\frac{b}{\sqrt{r_{r/n}l_{r/n}}}\left[f_{r/n}^{1/2} + 0.75\left(\frac{r_{r/n}}{l_{r/n}}\right)^{1/2} f + 0.14\left(\frac{r_{r/n}}{l_{r/n}}\right) f^{3/2}\right] \ln\left(\frac{0.158r_{r/n}}{r_0}\right) \tag{5}$$

where subscript r/n means the expression is either for the rod-shaped β″ precipitates or for the needle-shaped β′ precipitates, and r_0 denotes the inner cut-off radius (0.572 nm [44]) for calculation of the dislocation line tension.

It is well known that, if two or more types of strengthening obstacles are present in the matrix, the total critical resolved shear stress (CRSS), τ_t, of the materials will be a superposition of the strengthening effect of the individual type of strengthening obstacles, following the superposition law of either density-dependent $\tau_t^\alpha = \sum_{i=1}^N n_i^{\alpha/2}\tau_i^\alpha$ $\left(\sum_{i=1}^N n_i = 1\right)$ [30,31] or independent of density $\tau_t^\alpha = \sum_{i=1}^N \tau_i^\alpha$ [32–36], where τ_i is the contribution to the strengthening effect due to the i particles and n_i the density function of i particles, and the exponent α has the value between 1.0 (linear addition law) and 2.0 (Pythagorean addition law). Similarly, the two version of superposition law will both be used here to

model the coupling effect of multiple precipitates on σ_y, i.e.,

$$\sigma_y = \sigma_i + \sigma_{ss} + \left(\sum_j (\sigma_j)^\alpha\right)^{1/\alpha}, \quad j = s, r, n \tag{6-a}$$

$$\sigma_y = \sigma_i + \sigma_{ss} + \left(\sum_j (n_j)^{\alpha/2}(\sigma_j)^\alpha\right)^{1/\alpha}, \quad j = s, r, n \tag{6-b}$$

with Eq. (6-b) taking account of the weight effect of the relative volume fraction of the multiple precipitates $\left(\sum_{i=1}^{N} n_i = 1\right)$.

Calculations show that Eq. (6-a) cannot model the aging-dependent yield strength of present Al–Mg–Si alloys. On the contrary, Eq. (6-b) is found to describe the coupling effect of the multiple precipitates on σ_y satisfactorily. Fig. 5(a) and (b) shows the calculations using Eq. (6-b) (lines) compared with the experimental measurements (solid dots) at 473 and 523 K, respectively. At T = 523 K, calculations (solid line) match well with the experiments at α = 2.0 (Fig. 5(b)). At T = 473 K, however, calculations underestimate the yield strength even at α = 1.0 (Fig. 5(a)). Some revisions could be made on Eq. (6-b) when considering the *in situ* formation of β″ precipitates on the pre-β″ precipitates. Because of the slow growth of β″ precipitates at T = 473 K, the pre-β″ particles served as the nucleating sites for the β″ precipitates were not consumed entirely and so a β″ precipitate usually overlapped a partially dissolved pre-β″ particle (Fig. 6(a)). It is thus reasonable to incorporate the strengthening effect of the pre-β″ precipitates with that of the β″ precipitates. This means that the term of $(n_s + n_r)^{\alpha/2}(\sigma_s + \sigma_r)^\alpha$, instead of $n_s^{\alpha/2}\sigma_s^\alpha + n_r^{\alpha/2}\sigma_r^\alpha$, could be used in Eq. (6-b), which puts out calculations fitting well with the experimental results when α = 1.0, as shown in Fig. 5(a) as the solid line. At T = 523 K, however, the β″ precipitates grew fast by consuming the pre-β″ particles rapidly, overlapping of the two particles was seldom observed after t = 2 h (typically seen in Fig. 6(b)) and thus no modification should be made on Eq. (6-b).

The increase in exponent α from 1.0 to 2.0 with raising aging temperature from 473 to 523 K may be associated with the interaction effect of the multiple precipitates. When the rod-shaped β″ precipitates and the needle-shaped β′ precipitates both have larger sizes especially in the long dimension such as the case at 523 K, the strain fields of the precipitates or their hindrances to dislocation movement are easy to overlap and interact with each other. This will result in a Pythagorean addition law on the strengthening effect of the multiple precipitates. While at 473 K, the multiple precipitates, all in short sizes and with much less interaction, will contribute to the strength most separately, following an approximate linear addition law. Fig. 5(c) summarizes the appropriate calculations that are in good agreement with the experiments.

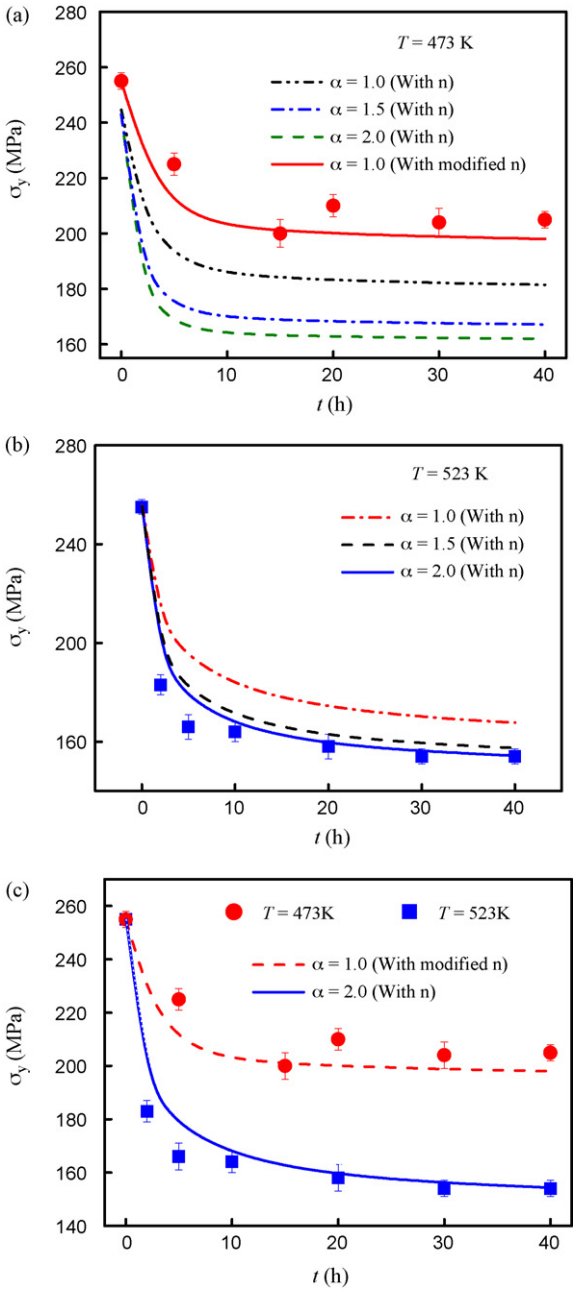

Fig. 5. Experimental and calculated dependence of yield strength (σ_y) on t at T = 473 K (a) and T = 523 K (b). Dots are experimental results and lines are calculations with α = 1.0, 1.5, and 2.0, respectively. Calculations fitting well with the experiments are summarized in (c).

4.2. Coupling effect of multiple precipitates on ductility

The ductility of commercial heat-treatable aluminum alloys is closely dependent on the second phase particles that include not only the nanometer-scaled precipitates but also submicrometer-scaled dispersoids and micrometer-scaled constituents [16–18]. A multiscale fracture model has been developed by the present authors [19–22] to describe the coupling effect of the differently scaled second phase particles on the strain to fracture, ε_f, of the samples as

$$\varepsilon_f = \frac{1}{\tilde{\varepsilon}_E(\theta)}\left[\frac{I}{0.405\pi h}\right]^{1/n+1}\left[\frac{\lambda_c}{2r_c} - 1\right]^{1/n+1}\frac{\sqrt{(\varepsilon_d)^2 + (\varepsilon_p)^2}}{2} \tag{7}$$

with

$$\varepsilon_d = 1.7 r_d b \frac{\lambda_p}{\lambda_d + \lambda_p}\rho_g^c \tag{8-a}$$

$$\varepsilon_p = 0.25\lambda_p b \frac{\lambda_d}{\lambda_d + \lambda_p}\rho_g^c \tag{8-b}$$

where r_i and λ_i (i = c, d, p) are the size and interparticle spacing of constituents, dispersoids, and precipitates, respectively, here the size and interparticle spacing of the constituents and dispersoids, i.e., r_c, λ_c, r_d, and λ_d, are regarded as constants during the secondary aging treatment and the their values have been given in [19]; ε_d is the local strain associated with the geometrically necessary dislocations caused by the incompatibility in shape change between

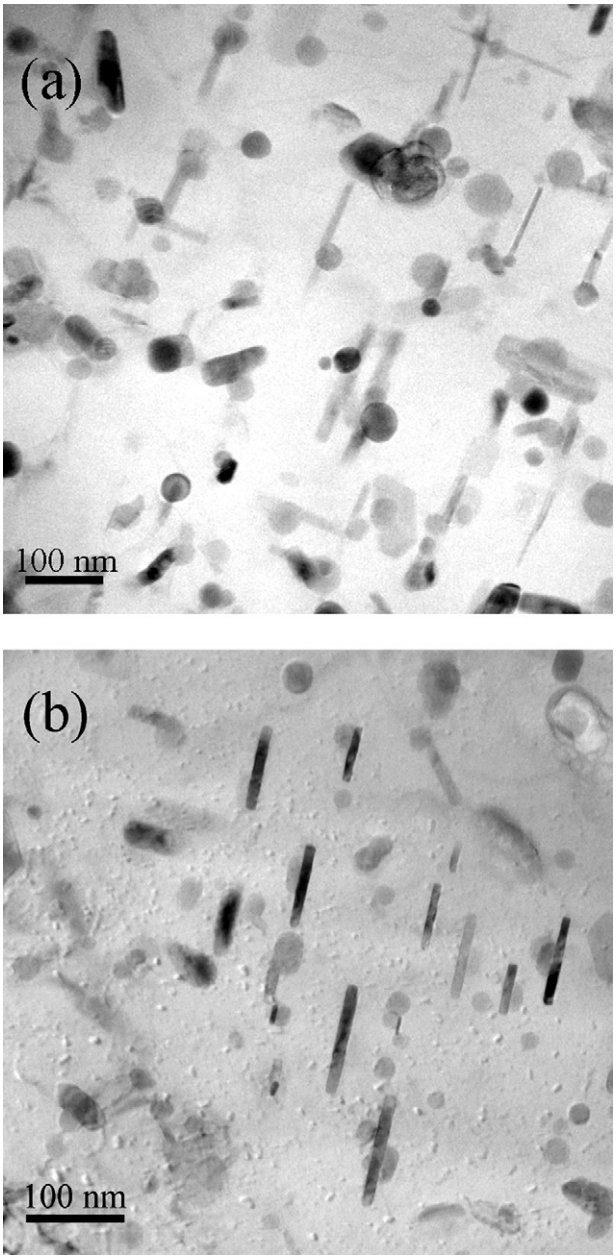

Fig. 6. Typical microstructure image of the sample aged at $T = 473$ K (a) and $T = 523$ K (b) for 2 h. The overlapping of β″ precipitates and partially dissolved pre-β″ particles is visible in (a) but seldom found in (b).

matrix and dispersoids in deformation, and ε_p is that related to the precipitates, ρ_g^c is the critical density of geometrically necessary dislocations in Al matrix; $\tilde{\varepsilon}_E(\theta)$ is the effective value for normalized coefficient $\tilde{\varepsilon}_{ij}(\theta)$ and is a constant when $\theta = 0$ (θ is the cylindrical coordinate angle of a point with respect to the crack tip), n is the strain hardening exponent and I and h are functions of n [19]:

$$I = 10.3\sqrt{0.13 + n} - 4.8n \tag{9-a}$$

$$h = \frac{3}{2\sqrt{1 + 3n}} \tag{9-b}$$

Because the absolute values of some parameters, such as ρ_g^c and $\tilde{\varepsilon}_E(\theta)$, are difficulty to determine while all of these parameters could be regarded as constants approximately, normalization treatment is usually employed [19–22] to eliminate these unknown parameters and to obtain the normalized ε_f. In this treatment, a reference strain to fracture (ε_f^R) should be chosen as the divisor. Here, ε_f^R is defined as the strain to fracture of the sample before the secondary aging treatment, which means that the normalized ε_f of the sample at $t = 0$ is 1.

Although the multiscale fracture model has been well applied to the commercial heat-treatable aluminum alloys, Eq. (7) is limited to a single kind of precipitates. When several kinds of precipitates are coexistent such as in present alloy, Eq. (7) should be modified to take account of the coupling effects of the multiple precipitates simultaneously. The ductility of aged aluminum alloys is closely dependent on the number of geometrically necessary dislocations induced by the precipitates. When multiple precipitates are presented, the geometrically necessary dislocations caused by the multiple precipitates will be either superposed or covered by an overwhelming one, depending on the relative size and interparticle spacing between the multiple precipitates. Therefore, a series of possible coupling effects of the multiple precipitates will be considered in modifying Eq. (7). In other words, the effect of a single kind of precipitates (Case I), two kinds of precipitates (Case II), and all the three kinds of precipitates (Case III) will be respectively considered one by one in modification on Eq. (7). Physically, Cases I, II, and III means that the ductility-related geometrically necessary dislocations come predominantly from one specific kind (s, or r, or n), two kinds (s + r, or s + n, or r + n), and all the three kinds (s + r + n) of the precipitates, respectively. Without loss of generality, simple density-free addition will be firstly consider and Eq. (7) is correspondingly rewritten as

$$\varepsilon_f = \frac{1}{\tilde{\varepsilon}_E(\theta)}\left[\frac{I}{0.405\pi h}\right]^{1/n+1}\left[\frac{\lambda_c}{2r_c} - 1\right]^{1/n+1}\frac{\sqrt{(\varepsilon_d)^2 + \sum_j(\varepsilon_j)^2}}{2},$$
$$j = s, \text{ and/or } r, \text{ and/or } n \tag{10}$$

$$\text{For Case I,} \quad \varepsilon_d = 1.7 r_d b \frac{\lambda_i}{\lambda_d + \lambda_i}\rho_g^c \tag{11-a}$$

$$\varepsilon_i = 0.25\lambda_i b \frac{\lambda_d}{\lambda_d + \lambda_i}\rho_g^c, \quad i = s, \text{ or } r, \text{ or } n \tag{11-b}$$

$$\text{For Case II,} \quad \varepsilon_d = 1.7 r_d b \frac{\lambda_i\lambda_j}{\lambda_d\lambda_i + \lambda_d\lambda_j + \lambda_i\lambda_j}\rho_g^c \tag{12-a}$$

$$\varepsilon_i = 0.25\lambda_i b \frac{\lambda_d\lambda_j}{\lambda_d\lambda_i + \lambda_d\lambda_j + \lambda_i\lambda_j}\rho_g^c,$$
$$(i, j) = (\text{s, r}), \text{ or } (\text{s, n}), \text{ or } (\text{r, n}) \tag{12-b}$$

$$\varepsilon_j = 0.25\lambda_j b \frac{\lambda_d\lambda_i}{\lambda_d\lambda_i + \lambda_d\lambda_j + \lambda_i\lambda_j}\rho_g^c \tag{12-c}$$

$$\text{For Case III,} \quad \varepsilon_d = 1.7 r_d b \frac{\lambda_i\lambda_j\lambda_k}{\lambda_d\lambda_i\lambda_j + \lambda_d\lambda_j\lambda_k + \lambda_d\lambda_i\lambda_k + \lambda_i\lambda_j\lambda_k}\rho_g^c \tag{13-a}$$

$$\varepsilon_i = 0.25\lambda_i b \frac{\lambda_d\lambda_j\lambda_k}{\lambda_i\lambda_d\lambda_j + \lambda_i\lambda_d\lambda_k + \lambda_i\lambda_j\lambda_k + \lambda_d\lambda_j\lambda_k}\rho_g^c,$$
$$(i, j, k) = (\text{s, r, n}) \tag{13-b}$$

In the above equations, ε_i (i = s, r, and n) indicates the local strain caused by spherical pre-β″ precipitates, rod-shaped β″ precipitates and needle-shaped β′ precipitates. Calculations show that, using the density-free addition of Eq. (10), all the above three cases or all

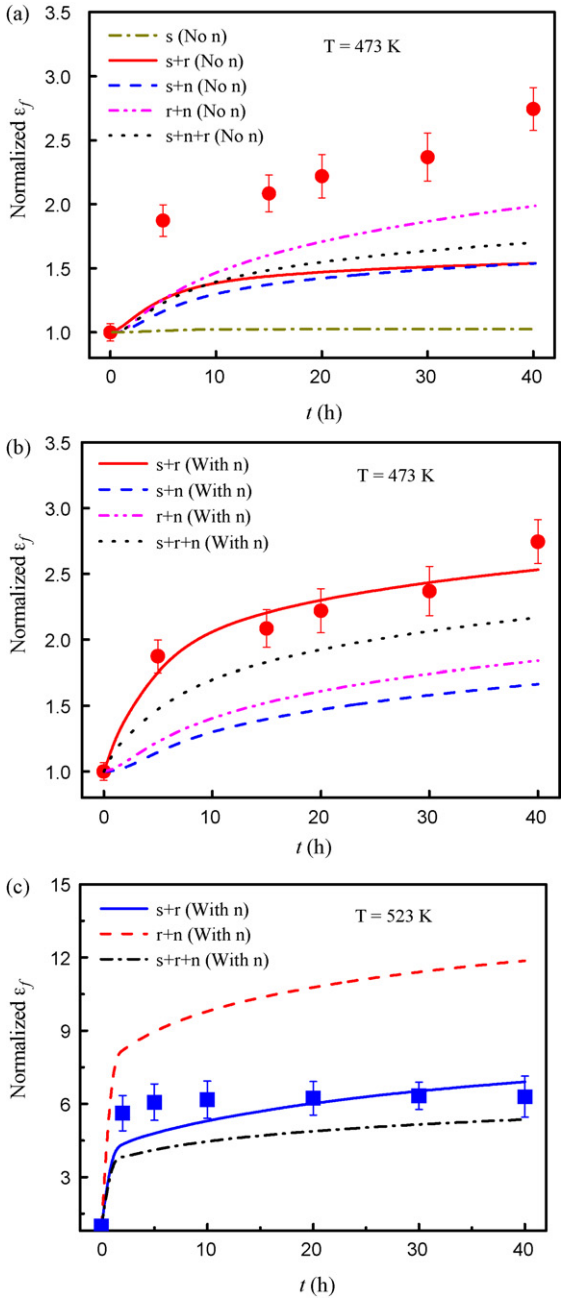

Fig. 7. Experimental and calculated dependence of the strain to fracture (ε_f) on t at T = 473 K (a and b) and T = 523 K (c). Dots are experimental results and lines are calculations. In (a), calculations are based on Eq. (10) without considering the density effect and some results of Case I (Eq. (11)), Case II (Eq. (12)), and Case III (Eq. (13)) are typically shown. In (b) and (c), calculations are based on the density-dependent Eqs. (14-a) and (14-b), respectively.

possible coupling effects of the multiple precipitates do not yield results in good agreement with the experiments, such as typically compared in Fig. 7(a) at T = 473 K.

Density-dependent addition is subsequently considered, similar to the modeling on yield strength (Eq. (6-b)). The weight effect of volume fraction of the multiple precipitates is thus taken into account in Eq. (10), yielding the following expressions:

$$\varepsilon_f = \frac{1}{\tilde{\varepsilon}_E(\theta)}\left[\frac{I}{0.405\pi h}\right]^{1/n+1}\left[\frac{\lambda_c}{2r_c}-1\right]^{1/n+1}\frac{\sqrt{\sum_j((\varepsilon_d)^2+n_j(\varepsilon_j)^2)}}{2} \quad (14\text{-a})$$

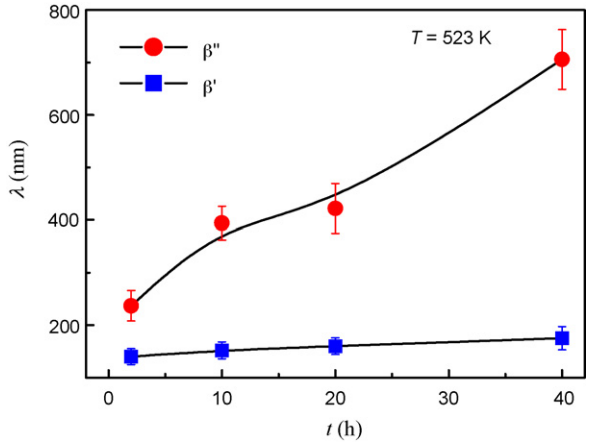

Fig. 8. Dependence of interparticle spacing of the β″ precipitates and β′ precipitates on t at T = 523 K.

or

$$\varepsilon_f = \frac{1}{\tilde{\varepsilon}_E(\theta)}\left[\frac{I}{0.405\pi h}\right]^{1/n+1}\left[\frac{\lambda_c}{2r_c}-1\right]^{1/n+1}\frac{\sqrt{\sum_j(n_d(\varepsilon_d)^2+n_j(\varepsilon_j)^2)}}{2},$$
$$j = s,\ \text{and/or}\ r,\ \text{and/or}\ n \quad (14\text{-b})$$

Eq. (14-a) is applied to the conditions where the interparticle spacing of the dispersoids is much larger than that of all the precipitates [21] such as at T = 473 K in present experiments (λ_d is about 500 nm and interparticle spacing of all the precipitates is less than 150 nm), while Eq. (14-b) is applied to the conditions where the interparticle spacing of the precipitates is on the same level of that of the dispersoids such as at T = 523 K in present experiments (λ_d is about 500 nm and interparticle spacing of β″ has a same level value). Similarly, Case II and Case III are respectively calculated one by one using Eq. (14) together with Eqs. (12) and (13). Some calculations including both Case II and Case III are typically shown in Fig. 7(b) and (c), compared with the measured values at T = 473 and 523 K, respectively. Comparisons indicate that the consideration of s + r could produce calculations fitting well with the experiments at both the aging temperature. This indicated that, among the three kinds of precipitates in present case, the spherical pre-β″ precipitates and the rod-shaped β″ precipitates should provide most geometrically necessary dislocations to affect the ductility. On the other hand, the ductility of the alloys is non-sensitive to the needle-shaped β′ precipitates because the β′ precipitates have much narrower interparticle spacing (Fig. 8) and so will induce less geometrically necessary dislocations [21,45–47]. The agreement between experiments and calculations at both T = 473 and 523 K shows that the superposition effect of multiple precipitates on the ductility is operative under different aging temperatures or different combinations of multiple precipitates. However, this superposition effect, although essentially similar to that on strength (Eq. (6-b)), is still somewhat different from the latter where all the precipitates make visible contributions.

At this moment, it is necessary to note that only the transgranular fracture is considered in present model because it is just the case predominantly observed in present experiment, see Fig. 9. When the weight of intergranular fracture is noticeable in the aged aluminum alloys [48], the ductility will be weaken and a much more complicated and comprehensive model should be developed to consider the influence of both the two fracture modes.

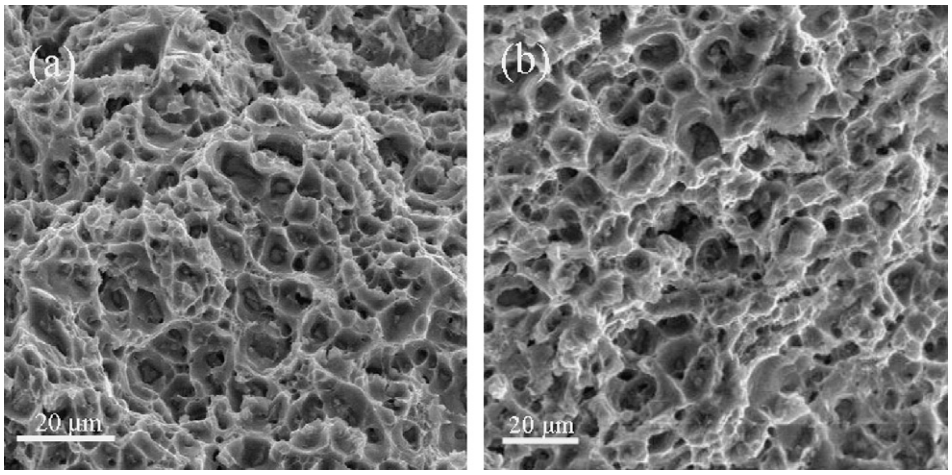

Fig. 9. Typically SEM image showing the dominant intragranular fracture mode in the samples aged at both $T = 473$ K (a) and $T = 523$ K (b).

5. Conclusions

Systematic experiments and modeling have been performed to study the coupling effect of multiple precipitates on the mechanical properties in Al–Mg–Si alloys that contain three kinds of strengthening particles, i.e., spherical pre-β″ precipitates, rod-shaped β″ precipitates, and needle-shaped β′ precipitates. Main conclusions are drawn as follows:

(1) All the three kinds of precipitates contribute to the yield strength and the coupling effect of the multiple precipitates on yield strength follows a density-dependent superposition law, $\left(\sum_i n_i^{\alpha/2}\sigma^{\alpha}\right)^{1/\alpha}$, which is in good agreement with recent computer calculations. The exponent α correspondingly rises from 1 to 2 with increasing the aging temperature from 473 to 523 K.
(2) The aging-dependent ductility or strain to fracture in the alloy is mainly related to the time evolution of the spherical pre-β″ precipitates and the rod-shaped β″ precipitates. A revised multiscale fracture model has been well developed to describe the aging-dependent ε_f quantitatively and it is clearly revealed that a density-dependent superposition law could also be applied to the coupling effect of multiple precipitates on the ductility, essentially similar to that on yield strength.
(3) The mechanical properties of the present Al–Mg–Si alloys are closely dependent on the combination of the multiple precipitates. An appropriate combination of the multiple precipitates, which can be achieved by artificially controlling the aging treatment, could improve the ductility even up to over six times while sacrificing the yield strength less.

Acknowledgments

This work was supported by the National Basic Research Program of China (Grant Nos. 2004CB619303 and 2005CB623700), the National Natural Science Foundation (50701035) and the National Outstanding Young Investigator Grant of China. This work was also supported by the 111 Project of China under Grant No. B06025, Program for Changjiang Scholars and Innovative Research Team in University (PCSIRT) as well as Science and Technology Key Project from Ministry of Education of China under Grant Nos. 02182 and 03182.

References

[1] E. Hornbogen, E.A. Starke Jr., Acta Metall. 41 (1993) 1.
[2] Ø. Grong, H.R. Shercliff, Prog. Mater. Sci. 47 (2002) 163.
[3] H.R. Shercliff, M.F. Ashby, Acta Metall. Mater. 38 (1990) 1789.
[4] H.R. Shercliff, M.F. Ashby, Acta Metall. Mater. 38 (1990) 1803.
[5] M.J. Starink, P. Wang, I. Sinclair, P.J. Gregson, Acta Mater. 47 (1999) 3855.
[6] M.J. Starink, S.C. Wang, Acta Mater. 51 (2003) 5131.
[7] O.R. Myhr, Ø. Grong, S.J. Andersen, Acta Mater. 49 (2001) 65.
[8] S. Esmaeili, D.J. Lloyd, W.J. Poole, Acta Mater. 51 (2003) 3467.
[9] W.J. Poole, D.J. Lloyd, J.D. Embury, Mater. Sci. Eng. A 234–236 (1997) 306.
[10] O.R. Myhr, Ø. Grong, Acta Mater. 48 (2000) 1605.
[11] A. Deschamps, Y. Brechet, Acta Mater. 47 (1999) 293.
[12] O.R. Myhr, Ø. Grong, H.G. Fjar, C.D. Marioara, Acta Mater. 52 (2004) 4997.
[13] A.W. Zhu, E.A. Starke Jr., Acta Mater. 47 (1999) 3263.
[14] M. Nicolas, A. Deschamps, Acta Mater. 51 (2003) 6077.
[15] G. Liu, G.J. Zhang, X.D. Ding, J. Sun, K.H. Chen, Mater. Sci. Eng. A 344 (2003) 113.
[16] J.T. Staley, Aluminum 55 (1979) 277.
[17] G.T. Hahn, A.R. Rosenfield, Metall. Trans. A 6 (1975) 653.
[18] G.G. Garrett, J.F. Knott, Metall. Trans. A 8 (1978) 1187.
[19] G. Liu, J. Sun, C.W. Nan, K.H. Chen, Acta Mater. 53 (2005) 3459.
[20] G. Liu, G.J. Zhang, R.H. Wang, W. Hu, J. Sun, K.H. Chen, Acta Mater. 55 (2007) 273.
[21] G. Liu, G.J. Zhang, X.D. Ding, J. Sun, K.H. Chen, Metall. Mater. Trans. A 35 (2004) 1725.
[22] G. Liu, G.J. Zhang, X.D. Ding, J. Sun, K.H. Chen, Mater. Sci. Technol. 19 (2003) 887.
[23] D.L. Gilmore, E.A. Starke Jr., Metall. Mater. Trans. A 28 (1997) 1399.
[24] W.A. Cassada, G.J. Shilfet, E.A. Starke Jr., Metall. Trans. A 22 (1991) 287.
[25] E. Clouet, L. Lae, T. Epicier, W. Lefebvre, M. Nastar, A. Deschamps, Nat. Mater. 5 (2006) 482.
[26] C.S. Tsao, C.Y. Chen, U.S. Jeng, T.Y. Kuo, Acta Mater. 54 (2006) 4621.
[27] D.J. Chakrabarti, D.E. Laughlin, Prog. Mater. Sci. 49 (2004) 389.
[28] X. Wang, W.J. Poole, S. Esmaeili, D.J. Lloyd, J.D. Embury, Metall. Mater. Trans. A 34 (2003) 2913.
[29] C. Ravi, C. Wolverton, Acta Mater. 52 (2004) 4213.
[30] A.W. Zhu, A. Csontos, E.A. Starke Jr., Acta Mater. 47 (1999) 1713.
[31] A.J. Ardell, Metall. Trans. A 16 (1985) 2131.
[32] B.C. Lee, J.K. Park, Acta Mater. 46 (1998) 4181.
[33] R.A. Karnesky, L. Meng, D.C. Dunand, Acta Mater. 55 (2007) 1299.
[34] J.C. Huang, A.J. Ardell, Acta Mater. 36 (1988) 2995.
[35] C. Schlieser, E. Nembach, Acta Metall. Mater. 43 (1995) 3983.
[36] L.M. Brown, R.K. Ham, in: A. Kelly, R.B. Nicholson (Eds.), Strengthening Methods in Crystals, Elsevier, Amsterdam, 1971, p. 9.
[37] S.P. Yuan, G. Liu, R.H. Wang, X. Pu, G.J. Zhang, J. Sun, K.H. Chen, Scripta Mater. 57 (2007) 865.
[38] J.H. Chen, E. Costan, M.A. van Huis, Q. Xu, H.W. Zandbergen, Science 416 (2006) 312.
[39] D.W. Pashley, M.H. Jacobs, J.T. Vietz, Philos. Mag. A 16 (1967) 51.
[40] J.W. Edington, Practical Electron Microscopy in Materials Science, Van Nostrand Reinhold Company, London, 1976, p. 207.
[41] R.H. Wang, Q. Chen, B.L. Wang, S. Zhang, L.M. Peng, Appl. Phys. Lett. 86 (2005) 133101.
[42] G. Liu, Ph.D. Thesis, Xi'an Jiaotong University, 2002.
[43] F.R.N. Nabarro, Theory of Crystal Dislocation, Oxford University Press, Oxford, 1967.
[44] P.M. Kelly, Scripta Metall. 6 (1972) 647.
[45] M.F. Ashby, Philos. Mag. 21 (1970) 399.
[46] L.M. Brown, W.M. Stobbs, Philos. Mag. (1976) 351.
[47] K.C. Russell, M.F. Ashby, Acta Metall. 18 (1970) 891.
[48] S. Esmaeili, L.M. Cheng, A. Descamps, D.J. Lloyd, W.J. Poole, Mater. Sci. Eng. A 319 (2001) 461.